Hindawi
Advances in Civil Engineering
Volume 2023, Article ID 9969802, 17 pages
https://doi.org/10.1155/2023/9969802

Research Article

Failure and Acoustic Emissions of Coal–Rock Combinations with Different Dip Angles in the Shaqu No. 1 Coal Mine

Yuping Fu,[1,2] Yongliang He ,[1,2] and Chuantian Li[1,2]

[1]*School of Engineering for Safety and Emergency Management, Taiyuan University of Science and Technology, Taiyuan 030024, China*
[2]*Intelligent Monitoring and Control of Coal Mine Dust Key Laboratory of Shanxi Province, Taiyuan University of Science and Technology, Taiyuan, Shanxi 030024, China*

Correspondence should be addressed to Yongliang He; hyl@tyust.edu.cn

Received 16 October 2023; Revised 25 November 2023; Accepted 8 December 2023; Published 26 December 2023

Academic Editor: Dawei Yin

Copyright © 2023 Yuping Fu et al. This is an open access article distributed under the Creative Commons Attribution License, which permits unrestricted use, distribution, and reproduction in any medium, provided the original work is properly cited.

The force and deformation characteristics of the rock layer on the top and bottom of the coal seam change significantly when the dip angle changes. The mechanical properties and damage characteristics of differently inclined coal–rock assemblages were investigated, and the results were combined with acoustic emission information, including acoustic emission ringdown counts, to quantify the damage of inclined coal–rocks under compression. The experimental results showed that the stress–strain curves of the inclined coal–rock assemblages had four main stages, with approximately similar curves in the early stage and deformation in the later stage. The damage gradually changed from shear damage to interfacial slip damage, and the damage area gradually transitioned to the structural surface from coal body components. The cumulative acoustic emission energy tended to decrease with increasing inclination angle, and the peak acoustic emission energy gradually decreased. When the inclination angle was less than 30°, the cumulative energy of acoustic emissions increased slowly, then decreased, and it finally decreased significantly between 30° and 45°; from 0° → 15° → 30° → 45°, the energy change rates were +3.0%, −25.1%, and −78.2%, respectively. For coal–rock assemblages with different interfacial angles, the sliding damage instability caused by the coal–rock interface increased with increasing interfacial angle within the assemblage. The results of this study provide a deeper understanding of the mechanical properties of coal–rock assemblages with different inclinations and the characteristics of fissure extension. The fractal dimension based on particle number decreased with increasing loading rate, and the larger the loading rate was, the smaller the fractal dimension. In addition, the current findings provide a reliable foundation for further understanding the mechanisms of disasters caused by coal–rock disturbances, such as excavation of inclined roadways and extraction of gas, as well as supporting the development of methods for monitoring, early warning, and prevention and control of these types of disasters.

1. Introduction

Coal has been China's main energy source for a long time; with the depletion of shallow coal resources, mining has gradually shifted to greater depths, but the geological conditions and conditions in deep coal seams tend to be complex [1, 2]. Deep mining and shallow mining primarily differ on the basis of the special geological environments of deep rock masses, i.e., complex mechanical environments consisting of three highs and one disturbance": high-geopathic stress, high-karst water pressure, high-gas pressure, and mining disturbance [3, 4]. With increasing coal mining depth, engineering disasters such as roadway deformation and instability, roof collapse, and rock bursts occur frequently in underground mining [5–7]. Disasters in deep coal mining are affected by the fractured structural planes of coal and rock, and they are the result of the joint action of "coal–rock" combined structures [8, 9]. The main reason for the occurrence of rock burst disasters is that the mechanical system composed of engineering geological bodies is completely unstable [10, 11]. Therefore, it is of great significance to study the failure mechanism of coal–rock combinations to prevent mine disasters [12]. A mine is affected not only by the physical and mechanical

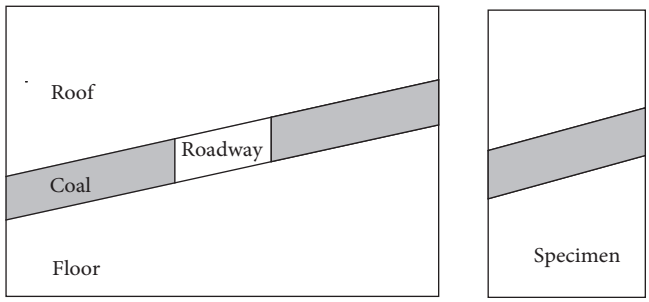

Figure 1: Coal–rock combination model.

properties of individual coal or rock bodies but also by the mechanical properties of the combined coal and rock structure. Underground engineering projects, especially coal mine roadways, are affected by different coal and rock combinations. Underground engineering is usually conducted in layered strata with different lithologies and stress states, and the coal–rock composite engineering body is a composite engineering structure composed of monolithic coal and monolithic rock. The mechanical properties of the composite structure are quite different from those of a single coal body or rock body. Many practical engineering efforts and research studies have shown that the root cause of coal mine impact disasters is the overall destruction and destabilization of the composite coal–rock and engineering structure system under the action of strong stress disturbance. In actual production, the coal seam and rock stratum sometimes incline, which has a greater impact on the stability of the top and bottom surfaces, as shown in Figure 1. In inclined coal seam, the coal seam forms a certain angle with the top and bottom plate. Inclined coal seam brings some harm to rock burst and other problems.

Extensive research has been conducted on the mechanical properties of model coal–rock composites [13]. The mechanical properties of the coal and rock mass are closely related to the physical properties of the component masses; however, they are also related to many external factors. Many scholars have conducted preliminary research on the mechanical properties of composite coal and rock samples. Regarding the static mechanical properties of a composite (coal) rock mass, Li et al. [14] studied the shear behavior of the coal–rock interface and analyzed acoustic emission signals during the test. They found that the coal–rock interfacial strength was mainly affected by the coal–rock strength. Liu et al. [15] proposed an experimental method to obtain the stress and strain of coal in coal–rock composite samples by using strain gauges. They conducted tests on 13 coal–rock composite samples, revealing the influence of rocks in coal–rock samples on the mechanical behavior of coal. Jin et al. [16] reported a strong positive correlation between the plastic strain of loaded coal and rock and the characteristic acoustic emission parameters. These research results have important theoretical and practical significance for further studying the acoustic emission signal characteristics of coal and rock during loading damage and for predicting dynamic coal and rock disasters. Ma et al. [17] used PFC software to explore the differences in the mechanical and energy evolution characteristics of composite samples of different coals and rocks with high ratios. The results showed that the smaller the coal-to-rock height ratio was, the greater the elastic modulus, and the higher the peak strength, with an exponential relationship with the coal-to-rock height ratio. The peak strain decreased linearly with the reduction in the coal-to-rock height ratio. Wang et al. [18] conducted a permeability stress test on a single fractured coal–rock combination. With increasing effective stress, the permeability and stress sensitivity of the single fractured coal–rock combination gradually decreased. The permeability of the coal–rock combination depended on the lower permeability value of the two components. Guo et al. [19] studied the failure mechanism and acoustic emission characteristics of coal–rock combinations with different coal–rock ratios and conducted uniaxial compression tests and acoustic emission tests for three coal–rock combinations with coal–rock ratios of 1 : 2, 1 : 1, and 2 : 1. With increasing coal–rock ratio, the failure degree of the test piece gradually decreased, and the fracture form gradually changed from fragmentation to collapse. Wang et al. [20] conducted conventional triaxial compression tests on coal–rock combinations with different high coal–rock ratios, studied the stress and deformation characteristics of coal–rock combinations, and analyzed the test results under different strength criteria. Huang and Liu [21] analyzed the influence of the loading and unloading rate and path on the mechanical properties of composites of coal and rock. With increasing loading rate, the strain increase in the coal and rock composites in the elastic stage, plastic stage and failure stage gradually increased, and the peak point strain showed a linear upwards trend. Ma et al. [22] used the split Hopkinson pressure bar (SHPB) system to analyze the dynamic mechanical properties of a coal–rock combination composed of limestone, shale, sandstone, bituminous coal and anthracite. The dynamic compressive strength and elastic modulus of the coal–rock combination were less than the average values for single rock and coal, while the limit strain and strain rate of the coal–rock combination were greater than the average values for single rock and coal. Zhang and Wang [23] analyzed the influence of stress level and infiltration time on the creep characteristics of coal and rock. With increasing infiltration time, the water content of coal and rock increased and tended to become stable, and the uniaxial compressive strength gradually decreased. The established model reflected the whole process of creep deformation and the failure of permeable coal and rock. Li et al. [24] studied the damage law and mechanism of coal–rock joint structures under the action of liquid nitrogen, established physical and mechanical models of freeze–thaw damage, analyzed the impact of ice wedge expansion stress on coal–rock joint structure damage, and established damage criteria. Zhang et al. [25] conducted uniaxial compression tests and Brazilian splitting tests on coal–rock combinations, where the stress threshold for crack initiation and damage in coal–rock combinations increased with increasing coal–rock height ratio. Gong et al. [26] studied the effect of fast loading rates on the mechanical properties of coal–rock bonds and analyzed the stress–strain curves, dynamic peak stress–strain, elastic modulus, and energy distribution laws of coal–rock bonds at different loading rates. Lu et al. [27] proposed a dynamic difference-based generative adversarial network (DDGAN) that used a composite objective function to supervise and guide the network for

coal–rock fracture evolution prediction. Wu et al. [28] used realistic failure process analysis (RFPA) to perform uniaxial compression tests on coal rocks containing calcite veins at different dip angles. Different azimuths of the calcite veins altered the internal stress distribution of the coal body, resulting in greater compressive strength at low dips (0°, 15°, and 30°). Xia et al. [29] conducted a numerical simulation of a coal–rock combination using the particle flow code PFC2D to analyze its mechanical damage behavior, acoustic emission (AE) properties, and damage characteristics. In previous related studies, the mechanical properties, damage modes, damage mechanisms, and impact tendencies of single coal bodies, rock bodies, or complete coal–rock assemblages have been extensively studied, and the results of corresponding indoor mechanical tests and theoretical analyses have proven that the mechanical response of coal–rock assemblages is significantly different from that of pure coal or rock bodies [30, 31]. Rock bursts, coal and gas protrusion, roof collapse, impact ground pressure, and other underground disasters lead to destabilization and damage of the rock structure. The destruction mechanism and process are complex and variable; not only is a single rock structure affected, but many composite rock layers affect each other as a result of mechanical interactions within the system [32, 33]. Huang et al. [34] investigate the relationships between the rock mechanical properties, fractal dimensions, and homogeneity. Li et al. [35] studied the fractal dimensions of solid phase, pore phase, and interface between them by box counting method based on digital rocks. He et al. [36] developed a fractal model to quantify the rock strength based on the fractal dimensions of grain size and grain aspect rat. Assessment of the occurrence and mechanism of these dynamic disasters cannot consider only the mechanical behavior of a single structure, but should take into account the overall structure. Based on this viewpoint, many scholars at home and abroad have conducted a large number of experimental studies on the mechanical behavior of coal–rock assemblages. Coal–rock assemblages are composite structures formed by the combination of coal and rock bodies with different mechanical properties, and they the component bodies be combined in various ways, such as by natural coring and postprocessing bonding. However, due to the low strength of the bonding surface, test samples are often used in postprocessing mode, which is relatively simple and convenient. Coal–rock assemblages are naturally different from single rock bodies in terms of mechanical properties due to their different compositional structures. Scholars at home and abroad have conducted much research on the above problems, and the existing research mainly focuses on coal–rock composite bodies. Due to the complexity of the formation and evolution of underground engineering structures, the mechanical behavior of inclined coal–rock composite bodies will have a significant impact on the mechanical behavior of the engineering structures, in turn influencing the mechanical response characteristics. However, there are few studies on the physical and mechanical properties and damage mechanisms of inclined coal–rock composites. The interface inclination angle of coal–rock assemblage has a key influence on its mechanical strength. With the increase of the interface inclination angle of coal–rock assemblage, the compressive strength and elastic modulus of coal–rock assemblage both decrease, and the strength loss of coal–rock assemblage specimens is aggravated by cyclic stress loading, and the coal–rock mass structure is more prone to instability failure in the environment of cyclic stress [37].

Scholars at home and abroad have conducted many studies on pure coal, pure rock, and coal–rock assemblages without inclination and achieved some research results. An inclined coal–rock assemblage is a combination of a coal body and a rock body with a certain inclination angle to each other. Coal and rock bodies have very discrete and inhomogeneous natures, which causes large errors in the results of experimental studies of coal–rock assemblages. In this study, acoustic emission characteristics and fissure extension damage were analyzed using uniaxial compression tests of coal–rock assemblages with different inclination angles. A uniaxial compression test was conducted, and an acoustic emission system was used for data monitoring and acquisition during the compression process to obtain the mechanical properties of the assemblage specimens under uniaxial compression, elucidate the fissure extension process, and determine the characteristic changes in acoustic emissions. Through analysis of the influence of coal–rock assemblages with different inclination angles on the compression strength, modulus of elasticity, acoustic emission counts, and change in energy of assemblage specimens, the mechanical properties and emission characteristics of assemblages of different types of coal rocks were researched.

2. Materials and Methods

2.1. Specimen Preparation. The coal and rock samples used in this test were taken from the coal seam and roof of the Shaqu No. 1 coal mine of Huajin Coking Coal Co. According to the standards of the International Rock Mechanics Society, the coal and rock masses were cut into cubes with dip angles by rock cutting machines. The coal seam belonged to the No. 3 coal seam, with a depth of ~500 m, thickness of 3.0–6.5 m (average ~4.3 m), and a certain dip angle. The top rock was medium to fine sandstone, 10-m thick, mainly quartz sandstone, followed by feldspar. A drill rig was used to core the coal and rock bodies. The size of the drill rod of the coring machine was φ 50 mm. After the core was cut and polished on the rock cutting machine, the angle was processed using a premade angle mold, and then the same direction was used for polishing. The nonparallelism at each end of the specimen was required to be not greater than 0.03 mm, and the deviation of the diameter at each end was required to be not greater than 0.02 mm [38].

Three main factors influenced the changes in the coal seam and overlying rock strata in the Shaqu No. 1 coal mine: (1) changes in the thickness of the coal seam and overlying rock strata; (2) changes in the strength of the coal seam and overlying rock strata; and (3) changes in the dip angle of the coal seam and overlying rock strata. In engineering practice, coal tunneling types are classified as along the coal seam, along the bottom, along the top, or in the bottom of the tunnel because thick coal seams generally stay in the bottom of the coal roadway. As the bottom plate leaves part of the bottom coal with low strength and no

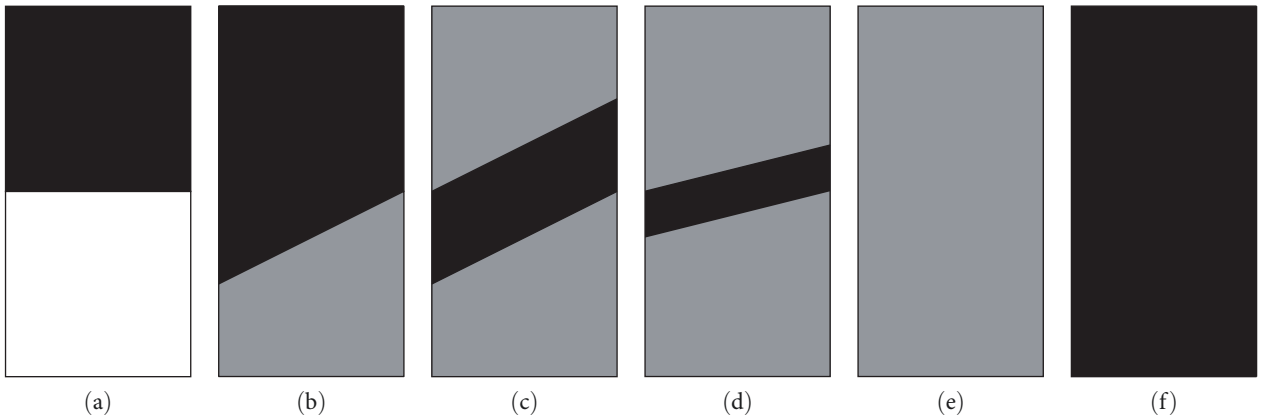

Figure 2: Sample diagram. (a) 0°, (b) 45°, (c) 30°, (d) 15°, (e) pure rock, and (f) pure coal.

support, the stress redistribution process easily damages the surrounding rock, triggering significant underground disasters. Due to the thickness of the coal seam with a certain inclination, the top plate rock is medium and fine sandstone, with quartz sandstone as the main rock, followed by feldspar. Coal samples were taken within 1–3 m from the roof; roof rock samples were taken within 1–2 m from the coal seam. First, a drilling machine was used to core the coal and rock body. After the core was taken, it was cut and polished on a rock cutter, and then the angle was processed by using a premade angle mold. Then, the same direction was used for polishing. In the long-term geological process, coal rock, as a sedimentary rock, has a certain layered structure, and there is usually a certain angle between the coalbed and the overlying rock layer. According to different depositional environments, four sets of specimens were fabricated to simulate coal–rock assemblages in different depositional environments by combining coal and rock at four inclination angles of 0°, 15°, 30°, and 45°. The interface between the coal and rock was bonded by adhesive, and the size of the model was 50 mm × 100 mm, as shown in Figure 2. The surface accuracy of the specimens after processing met the provisions of "Methods for Determining Physical and Mechanical Properties of Coal and Rock." To study the influence of rock strength on the energy evolution law of coal–rock combinations and explore the energy-driven failure mechanism of coal–rock combinations [39, 40], the test samples were divided into three groups: Group A was pure coal specimens, Group B was pure rock specimens (fine sandstone), and Group C was coal–rock combined specimens with a 1 : 1 ratio according to the coal seam condition; a white emulsion was used to combine the coal and rock specimens into 50 mm × 100 mm cubes. The coal and rock were combined at four dip angles of 0°, 15°, 30°, and 45° and used to simulate coal–rock assemblages from different depositionfigal environments. The rocks were taken from the fine sandstone of Group B. Both the pure coal and the coal in the combined specimens were taken from the same bulk coal. In the uniaxial primary loading tests, three specimens each of pure coal, muddy sandstone, and fine sandstone were used, and in the uniaxial cyclic loading tests, three specimens each of pure coal and fine sandstone and four to six specimens from Group C were used.

2.2. Experimental Systems. The uniaxial compression test equipment consisted of a loading control system, servo-hydraulic material testing machine and acoustic emission monitoring system, as shown in Figure 3. Coal and rock mass samples are processed to form coal–rock assemblage, and the coal–rock assemblage is pasted to form a whole. The coal–rock combination is put into the uniaxial compression testing machine, the acoustic emission probe is pasted around the coal–rock combination, the uniaxial compression testing machine is controlled by computer, and the acoustic emission signal is collected by the acoustic emission system. To obtain the relationship between the acoustic emission signal response and the specimen surface deformation field during loading, these test systems were activated at the same time to ensure synchronized acquisition of test data. The loading system for the uniaxial compression test was a servo-hydraulic controlled material testing machine with a maximum range of 2,000 kN, which could be used for displacement loading or speed loading. The uniaxial compression test was conducted in displacement-controlled loading mode with a loading rate set at 0.2 mm/min until the specimen was damaged, at which time loading was stopped. To minimize the end friction effect, a thin layer of lubricant was applied to the rigid metal plate placed on the specimen before applying the load. During the test, downward displacement of the upper loading plate indenter exerted pressure on the specimen, while the lower rigid loading plate indenter remained stationary. The acoustic emission system utilized a model PCI-2 acoustic emission testing device manufactured by the Physical Acoustics Inc. (United States of America), which is capable of detecting the internal damage development and fracture damage process of specimens during the testing process. Two acoustic emission sensors were attached to the coal and rock surfaces of the combined specimens. To monitor the acoustic emission signals realistically and effectively, petroleum jelly as a coupling agent was uniformly applied to the contact interface between the specimen

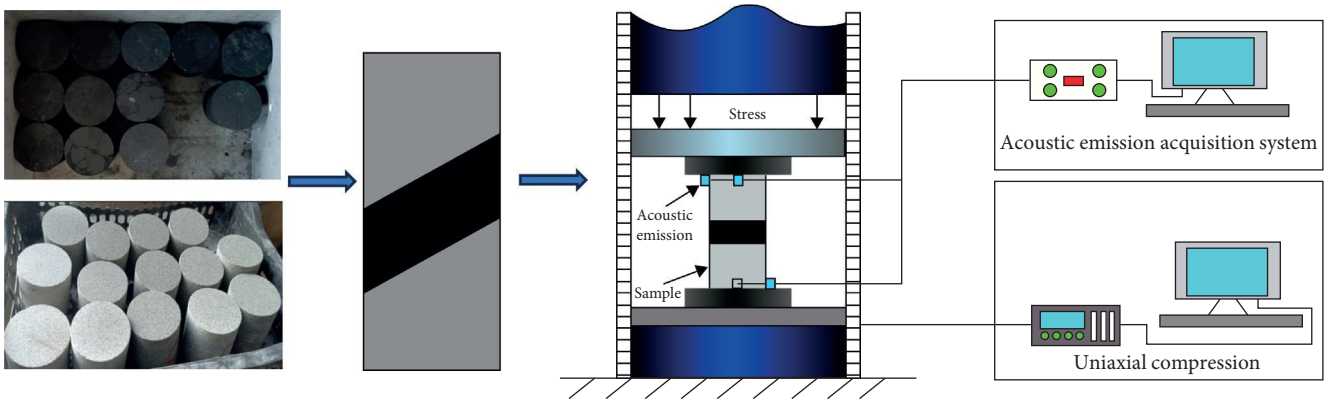

Figure 3: Experimental system.

and the sensors. The frequency of the acoustic emission detection sensor was set to 1 MHz. The acoustic emission signal recorded in the sensor was amplified and processed by a preamplifier. In addition, a specified threshold of 45 dB was set to prevent electronic or environmental noise in the test data [41–43]. To ensure effective coupling between the acoustic emission sensor and the specimen, the end of the acoustic emission probe was coated with petroleum jelly and held in place with a rubber band. During the test, the acoustic emission system was used to monitor the number and energy of acoustic emission events during cyclic loading. During the test, the loading and unloading system and acoustic emission system were synchronized to ensure that the systems had the same time parameters. Although there were some depressions and fissures on the surface of the samples, this did not affect the overall accuracy of the experimental results as uneven surfaces and long primary fissures were present in the actual subsurface rock formation.

2.3. Test Procedure and Program. Acoustic emission testing of the coal–rock assemblages was mainly conducted to determine the acoustic emission parameters during uniaxial compression of coal–rock assemblages with different angles. The acoustic emission signals monitored by the acoustic emission instrument were gain amplified, filtered and then transformed into a variety of quantitative acoustic emission parameters that were easy to understand and analyze. The basic acoustic emission parameters, such as ringdown count and energy, were recorded and analyzed by the methods such as single-parameter analysis, distribution map analysis, and correlation analysis to obtain the acoustic emission characteristics of the test object. The test process was as follows: (1) parameter setting: the uniaxial compression test machine loading parameters were set, and the acoustic emission system, consisting of a sensor, preamplifier, acoustic emission host, and display, was assembled. (2) Pretest calibration: to ensure the normal collection of acoustic emission signals during loading, the acoustic emission equipment was tested before each uniaxial compression test. (3) Specimen installation: it was ensured that the end surface of the coal–rock assemblage specimen was flat, and lubricant was applied on the two end surfaces of the specimen to reduce the end effect. An acoustic emission sensor was installed in the sample base of the universal testing machine with a coupling agent (petroleum jelly) and fixed with a leather band. (4) Testing and data recording: to ensure synchronization of the uniaxial compression data and acoustic emission data, the loading system and acoustic emission system were operated by two people. The operator of the acoustic emission system sent out the start command while pressing the start button. After the test started, the environment was kept as quiet as possible, and all data changes were observed. When the test reached the end condition, data acquisition was stopped at the same time, and the test data were saved.

The mechanical parameters, acoustic emission signals and surface deformation and damage characteristics of various types of specimens were obtained by conducting uniaxial compression tests on a series of pure rock specimens, pure coal specimens, and inclined coal–rock assemblage specimens with angles of 0°, 15°, 30°, and 45°. The damage modes of pure coal body specimens and pure rock bodies were typical shear damage modes. The damage mode of the complete coal–rock assemblage was dominated by tensile splitting, and there were many differences in the mechanical properties and damage modes between pure rock or pure coal specimens and fissure-type coal–rock assemblage specimens or complete coal–rock assemblage specimens. During the experiment, if one group of test data was obviously different from other groups of test data and the difference was relatively large, the test data of that group were eliminated. In addition, testing was continued under the same conditions until three or more similar results were obtained.

3. Uniaxial Compression Damage in Coal–Rock Assemblages with Different Dip Angles

3.1. Mechanical Parameters of the Coal and Rock Samples. The uniaxial primary loading test was conducted on single coal and rock specimens to obtain the basic mechanical parameters of the coal and rock for subsequent comparative analysis. The uniaxial primary compression test was load controlled with a loading rate of 1 kN/s until the specimen was damaged. Uniaxial cyclic loading tests were conducted on coal and rock, and assemblages to assess the energy evolution of the coal–rock assemblages. Uniaxial compression and deformation tests were conducted at 0.005 mm/s until

Table 1: Mechanical parameters of the coal and rock samples.

Category	Number	Uniaxial compressive strength (MPa)	Modulus of elasticity (GPa)
Coal	1-1	22.12	2.69
	1-2	23.65	2.66
	1-3	21.96	2.71
Rock	2-1	43.43	22.77
	2-2	44.14	21.65
	2-3	42.90	23.40

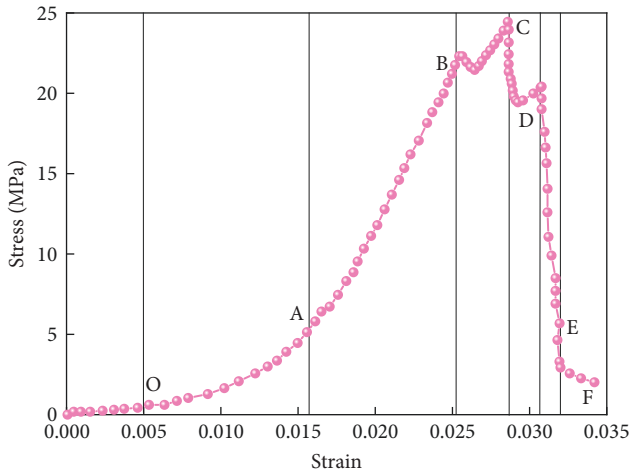

Figure 4: Coal stress–strain curve.

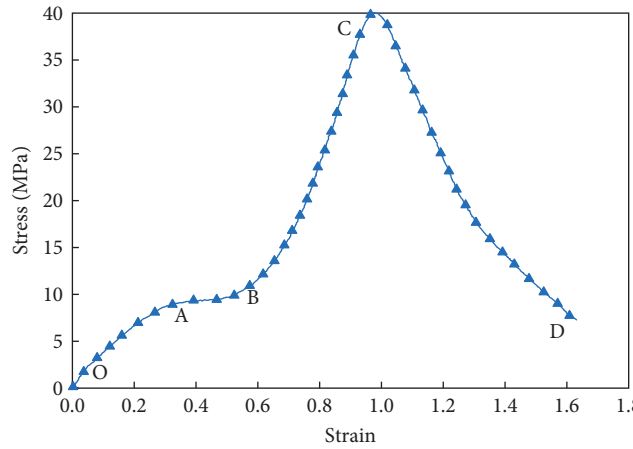

Figure 5: Rock stress–strain curve.

the specimens were destabilized. The specific mechanical parameters of the coal and rock are shown in Table 1.

3.2. Coal Damage under Loading. The stress–strain curve of the pure coal specimen during damage by loading is shown in Figure 4. The results showed significant nonlinearity in the damage process of the specimens under loading. As the stress increased, the degree of damage to the coal body rose, and at select moments, violent damage occurred; finally, destabilization fracture damage occurred. According to the stress–strain curve, the whole process of damage to the specimen under loading could be divided into five stages, as follows: (1) the OA compaction deformation stage was mainly characterized by the compaction closure and deformation of primary fractures and pores. As the strain increased, the stress increased slowly, but the rate of increase tended to increase. (2) The specimen underwent a long period before entering the AB section of the linear elastic deformation stage. The coherence with the compression-density stage was good, and its critical point was not easily distinguishable. (3) The BC section could be considered a continuation of the elastic deformation phase. (4) The specimen reached its peak stress at point C, marking the point at which the specimen reached the limit of its elastic energy storage and could no longer withstand higher stress levels. The specimen then entered section CD, corresponding to significant plastic deformation and the critical stage of destabilization damage. (5) In the DE destabilization phase, the stress was reduced significantly and rapidly, and the specimen lost its original load-bearing capacity. C was the critical loading point at which the specimen was able to withstand the maximum stress. With increasing loading, the internal structure of the specimen gradually lost its load-bearing capacity. Point D was the destabilization point of the specimen, where a significant reduction in stress occurred. The specimen lost its residual load-bearing capacity at the E damage point; there was dynamic damage, blocks were ejected and fell, and the stress curve showed an approximate "vertical" plunge.

3.3. Rock Damage under Loading. As shown in Figure 5, the stress–strain curve of sandstone could be divided into four stages. (1) In the OA compaction stage, the slope of the stress–strain curve was small, and the curve bent upwards. In this stage, due to the inelastic deformation caused by the compaction closure of the initial cracks and microcracks in the sandstone, the compaction degree of the cracks in the sandstone at low temperature was small. (2) In the AB elastic stage, the stress state of the rock specimen was lower than the yield state of sandstone. (3) In the BC plastic deformation stage, the slope of the stress–strain curve gradually bent downwards. With increasing strain, the sandstone specimen was gradually destroyed, and the yield strength of the material decreased. This was the plastic stage before yielding, and the specimen underwent extreme plastic deformation. In this stage, the microcracks in the sample gradually nucleated and diffused, and the stage ended at peak stress. (4) In the CD failure stage, the stress gradually decreased with increasing strain, and the stress–strain curve had a negative slope.

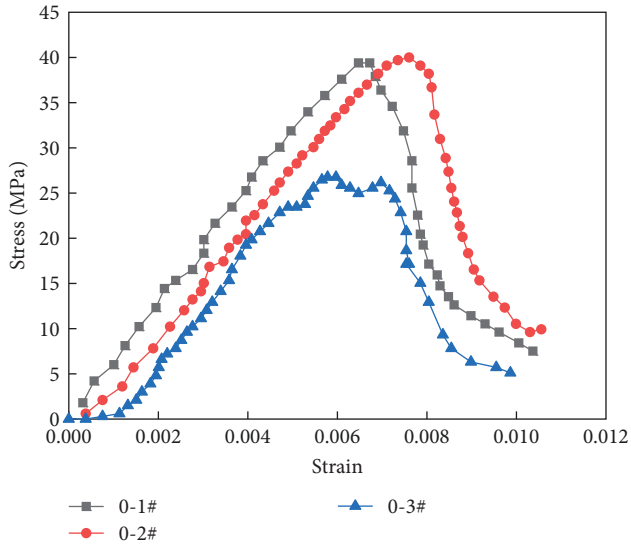

Figure 6: Stress–strain curve at 0°.

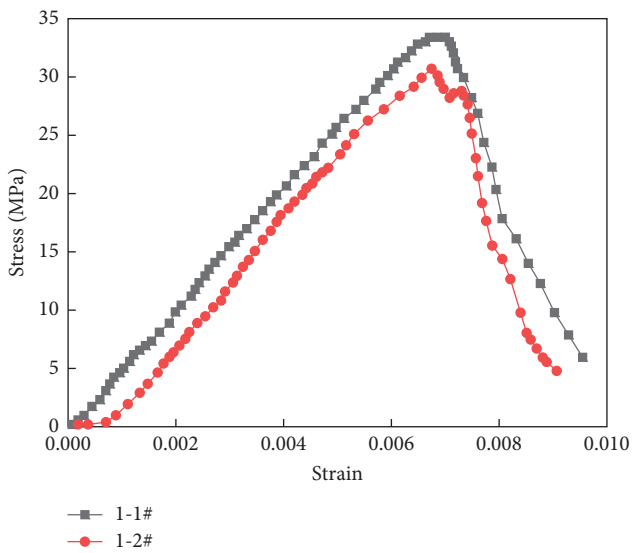

Figure 7: Stress–strain curve at 15°.

3.4. CoalRock Damage during Loading

3.4.1. Stress–Strain Curve at 0°. As shown in Figure 6, the uniaxial compressive strength of the coal–rock combination with a dip angle of 0° was relatively high, with a maximum compressive strength of 36 MPa. The rock in the combination was hardly damaged, and the coal body exhibited shear failure characteristics, mainly presenting X-type failure. The failure mode of the coal–rock combination with a dip angle of 0° was mainly brittle failure.

3.4.2. Stress–Strain Curve at 15°. As shown in Figure 7, the uniaxial compression test of the coal–rock combination with an inclination angle of 15° showed a uniaxial compressive strength of ~34 MPa, which was slightly lower than that of the 0° coal–rock combined specimen and lower than those of pure coal and pure rock. The dip angle of the coal–rock combination affected the shear strength of the shear plane, and the thickness of the coal and rock samples affected the scope of the coal and rock damage. The greater the thickness of the coal sample was, the more significant its damage, mainly because the elastic modulus of coal is less than the elastic modulus of rock. In the process of uniaxial compression, the elastic modulus of the coal was small, and the compressive strength limit was easily reached, which caused damage.

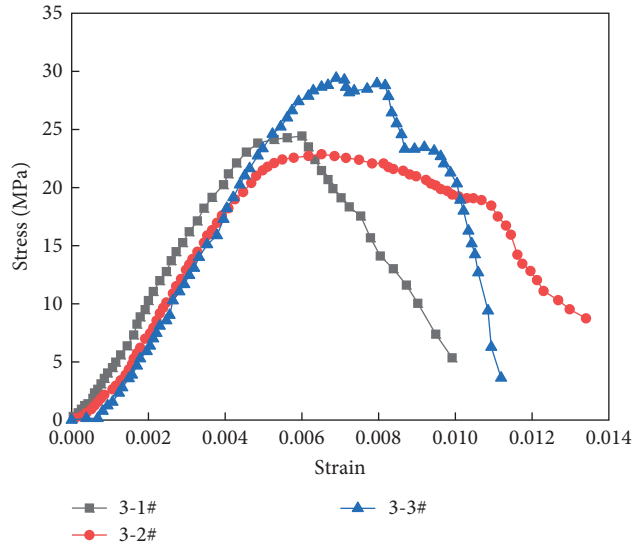

Figure 8: Stress–strain curve at 30°.

3.4.3. Stress–Strain Curve at 30°. As shown in Figure 8, in the process of uniaxial compression of the coal–rock combination with a 30° inclination, the ultimate compressive strength was 30.5 MPa, which was less than those of the coal–rock combinations with 0° and 15° inclinations. Under uniaxial compression, the 30° angle coal–rock combination exhibited compression shear and slip effects. The failure mode of this coal–rock combination was more affected by the coal–rock interface than were the 0° and 15° coal–rock combinations. The failure mode of the 30° coal–rock combination gradually shifted from brittle failure to ductile failure.

3.4.4. Stress–Strain Curve at 45°. As shown in Figure 9, the ultimate failure strength of the 45° inclined coal–rock combination during uniaxial compression was ~24 MPa, and the minimum ultimate failure strength was only ~18 MPa. The interface of this combination had a significant impact on the failure of the coal–rock mass. The failure of the coal–rock combination was mainly due to sliding, which also led to a decrease in bearing capacity. To prevent impact instability under this condition, it would be important to first prevent this type of sliding failure. The coal part remained intact, similar to the rock part after the specimen became unstable, indicating that the sliding of the interface between the coal and rock played a role in the failure of the inclined coal–rock mass.

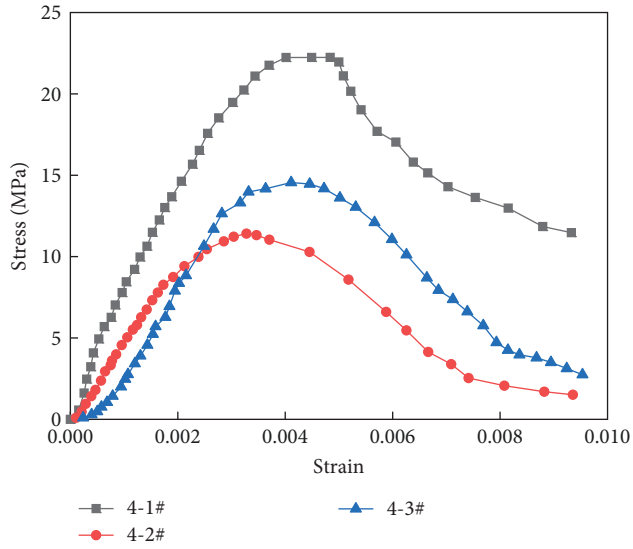

Figure 9: Stress–strain curve at 45°.

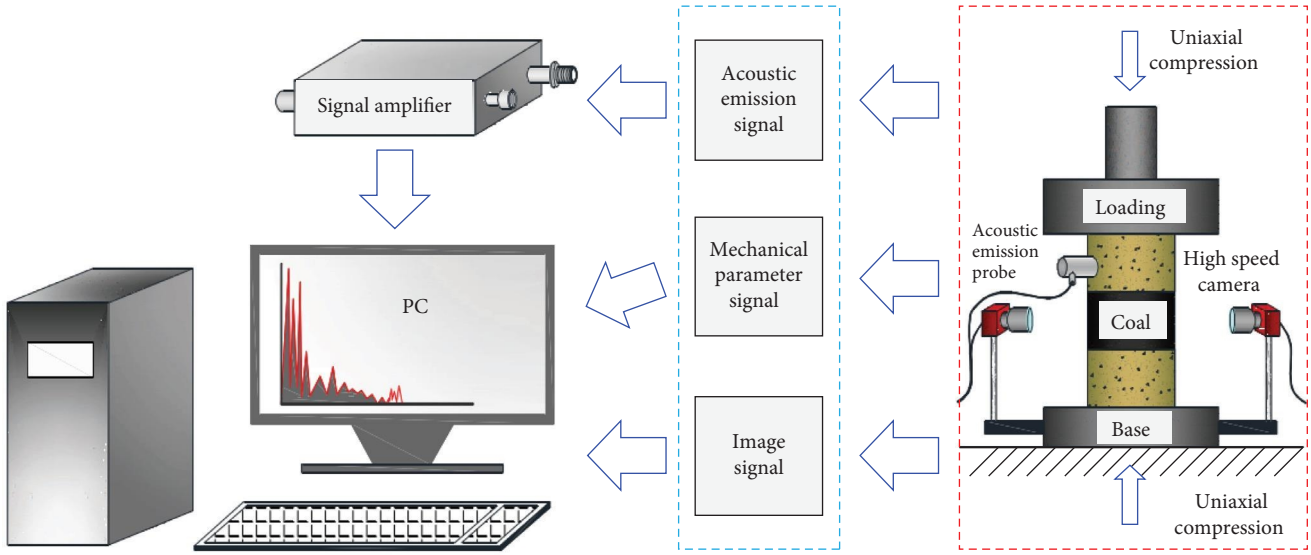

Figure 10: Uniaxial compression and acoustic emission test system for coal–rock composites.

4. Acoustic Emission Characteristics of CoalRock Combinations with Different Dip Angles

4.1. Acoustic Emission Characteristics. The mechanical properties of coal and rock masses are the foundation of engineering applications and design, and studying the mechanical properties of coal and rock masses, especially those of coal–rock combinations, is very important. A servo-hydraulic pressure testing machine, acoustic emission system, and high-speed camera were used to study the acoustic emission characteristics and crack patterns of coal–rock combinations with different inclinations. Figure 10 shows the uniaxial compression, acoustic emission, and crack propagation test system used.

The relationship between the acoustic emission ringdown count, cumulative ringdown count, and stress–strain curve of coal–rock combinations with different dip angles is shown in the figure. The acoustic emission ringdown count changed during the compaction and elastic stage of all coal–rock combinations. With increasing dip angle of the coal–rock combinations, the duration of acoustic emission increased, and the cumulative ringdown count exhibited a large and sudden change. As the interfacial angle of the coal–rock combination increased, the instability and failure of the entire coal–rock combination intensified due to failure of the interface. Sliding failure of the coal rock was caused by the interface between the coal and rock and the yield failure of the coal body.

Figures 11–14 show the temporal relationship between the acoustic emission energy and stress of coal–rock combinations with different dip angles. The coal–rock mass combination was greatly affected by changes in the inclination

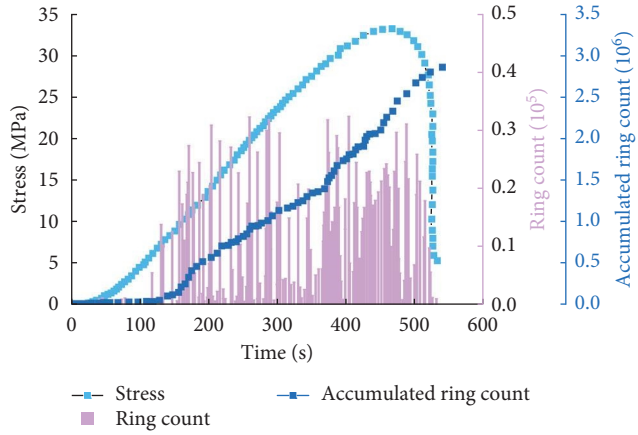

Figure 11: Acoustic emission characteristics of coal and rock with a 0° dip angle.

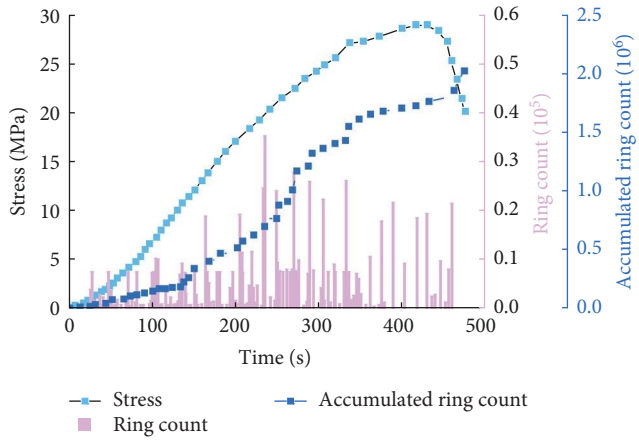

Figure 12: Acoustic emission characteristics of coal and rock with a 15° dip angle.

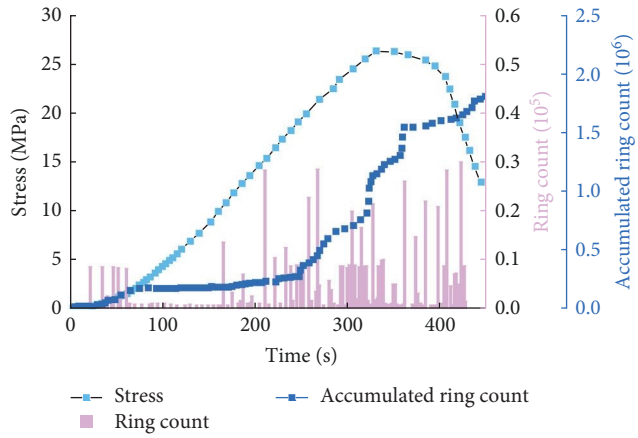

Figure 13: Acoustic emission characteristics of coal and rock with a 30° dip angle.

angle of the coal–rock mass. However, as the angle increased, the cumulative energy gradually decreased. When the inclination angle of the coal–rock mass was less than 45°, a series of acoustic emission energy changes occurred during the

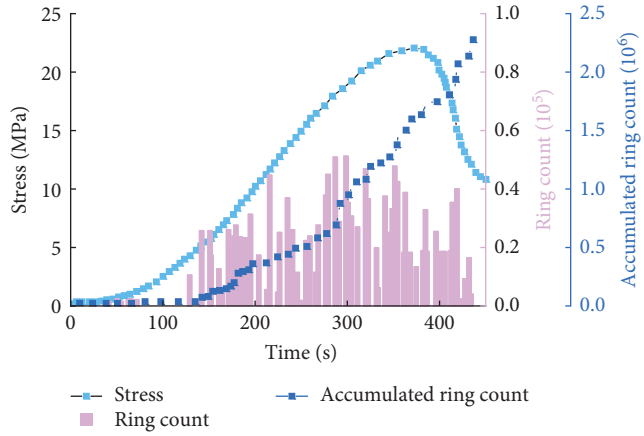

Figure 14: Acoustic emission characteristics of coal and rock with a 45° dip a ngle.

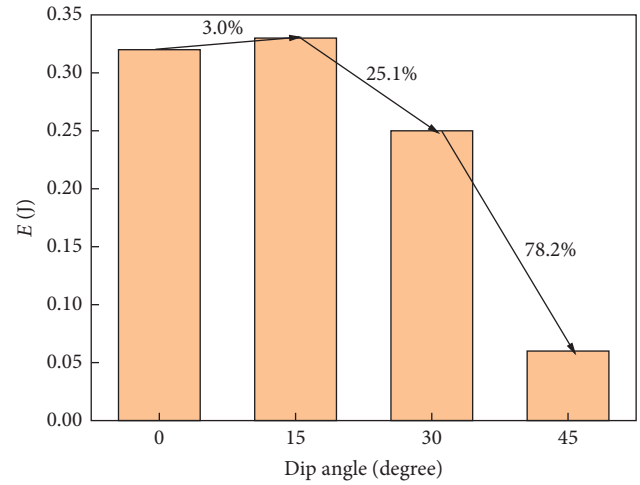

Figure 15: Cumulative acoustic emission energy of coal–rock combinations with different dip angles.

compaction and failure stages of the coal–rock mass combination. As the interfacial angle of the coal–rock combination increased, the cumulative acoustic emission energy curve showed a sudden "step". The pattern of this phenomenon was similar to that of ringdown count. Changes in the inclination angle of the coal–rock combination led to differences in the failure behaviors of the coal–rock combination. The larger the inclination angle was, the more severe the instability of the coal–rock combination, the greater acoustic emission ringdown count, and the greater the energy signal. Increases in the inclination angle of the coal–rock combination led to a decrease in specimen strength, resulting in a decrease in stored energy and an increase in the energy dissipated by the coal–rock combination.

4.2. Acoustic Emission Energy of CoalRock Combinations. The cumulative energy of acoustic emissions was used to characterize the energy changes during the failure process of the combinations. Figure 15 shows the cumulative energy of acoustic emissions of coal–rock combinations with

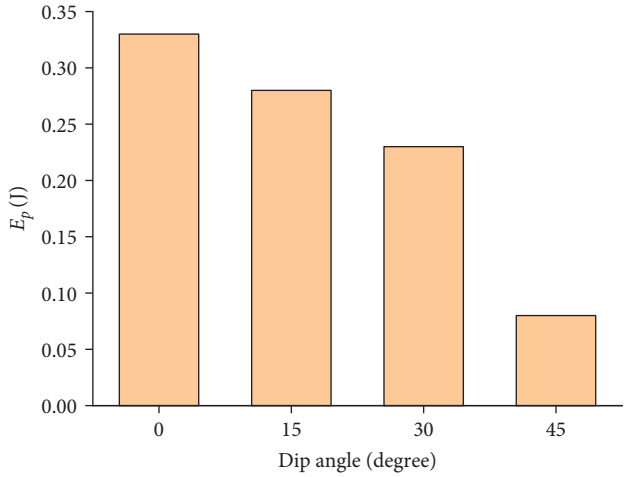

Figure 16: Peak acoustic emission energy of coal–rock combinations with different inclination angles.

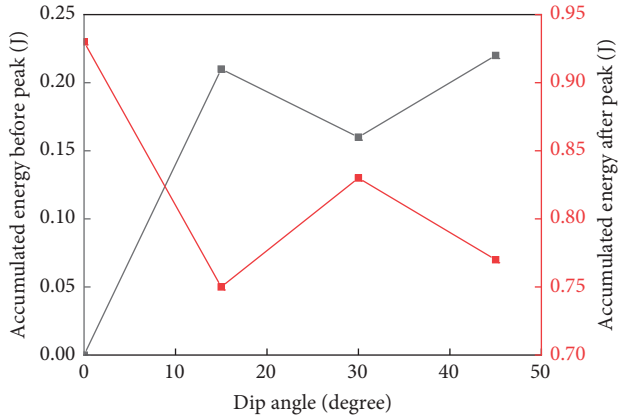

Figure 17: Cumulative energy ratio before and after the peak.

different dip angles. Overall, the cumulative energy of acoustic emissions showed a decreasing trend, mainly due to changes in the mechanical properties of the combinations due to the influence of the dip angle. When the inclination angle was less than 30°, the cumulative energy of acoustic emissions first slowly increased and then decreased, and a significant decrease was observed for angles between 30° and 45°. The reason for the significant decrease was a change in failure mode from predominantly shear failure to a combination of shear failure and interfacial sliding friction failure. In addition, the energy released during shear failure was greater than that released during sliding failure, resulting in a significant decrease in the cumulative energy of acoustic emissions.

Figure 16 shows the peak acoustic emission energy of coal–rock combinations with different dip angles, which exhibited a large amount of deformation and the most intense energy release at the peak time. The peak acoustic emission energy first slowly decreased, then rapidly decreased, and then slowly decreased with increasing inclination angle. Below an inclination angle of 30°, the ratio of peak energy to cumulative energy was quite large. It rapidly decreased between 30° and 45°, and the proportion remained at a relatively low level when the angle exceeded 45°.

Figure 17 shows the ratio of the cumulative energy of prepeak and postpeak acoustic emissions of coal–rock combinations at dip angles of 0°, 15°, 30°, and 45°. With respect to dip angle, the cumulative energy of prepeak acoustic emissions showed an overall trend of decreasing and then maintaining a steady decrease, while the cumulative energy of postpeak acoustic emissions showed an overall trend of increasing and then maintaining a steady increase. At an inclination angle below 15°, the cumulative energy before the peak decreased significantly. Between 15° and 45°, the cumulative energy before the peak remained within a reasonable range, and the cumulative energy continued to decrease significantly between 45° and 60°. The reason for the significant decrease was that the shear failure was the dominant factor between 0° and 15°, and the influence of the interface was small; this condition could be approximated by a single influencing factor of only shear failure. From 45° to 60°, sliding along the structural plane was approximately the only factor. From 15° to 45°, compression, shear, and sliding effects played a role. This behavior may have been influenced by the mean of the values for the component materials; moreover, the ratio of cumulative energy before the peak at an inclination of 30° was greater than that at an inclination of 15°. The cumulative energy of acoustic emission can also reflect the possibility of rock bursts in coal–rock combinations.

5. Failure of CoalRock Combinations with Different Angles under Uniaxial Compression

The failure mode of inclined coal–rock combinations is significantly different from the fracture evolution of pure coal rock. Therefore, studying the fracture evolution of different inclined coal–rock combinations is of great significance for understanding the failure behavior and mechanism of inclined coal–rock combinations, as well as the fracture process of inclined coal seam supports and mining operations. The entire process of crack propagation during the compression failure of coal–rock combinations with different dip angles was studied, the relationship between the main crack propagation characteristics and coal–rock fracture failure was analyzed, and the crack propagation relationships for different types of coal–rock combinations were obtained.

5.1. Destruction Phenomenon. The failure of inclined coal–rock combinations under uniaxial loading is shown in Figure 18. The middle of the coal rock in the dip coal–rock combination was damaged to varying degrees. The coal body underwent mainly X-shaped conjugate slope shear failure with a high degree of fragmentation, and multiple macrocracks ran through the whole coal sample. Although the rock in the combination was much stronger than the coal, almost all the rock underwent significant damage, mainly due to tensile failure, with a main crack. The rock block was relatively intact, and all the cracks in the rock were connected to the main damage in the coal body. The cracks near the coal body were relatively large, and the cracks had not penetrated the rock. The cracks developed from the coal–rock joint to the upper part of the rock, indicating that during the process

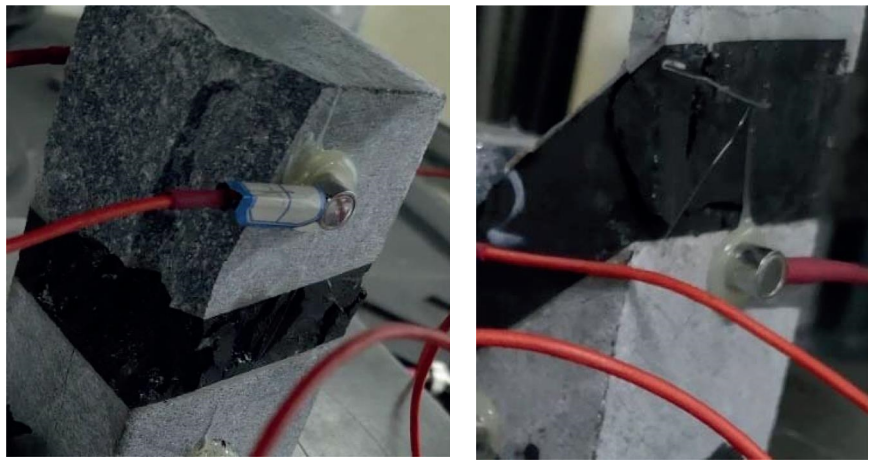

(a) (b)

Figure 18: Failure of inclined coal–rock combinations under uniaxial loading. (a) 15° and (b) 45°.

of compression of the coal–rock combination, coal was the first fractured body, which was the main factor controlling the strength of the composite test piece. The rock was destroyed before reaching its strength limit. From the analysis of the failure form and crack starting position of the rock, the main reason for rock failure may have been rapid crack expansion and the sudden release of elastic energy in the coal, which corresponded to instability failure driven by energy. When the angle of the coal–rock combinations at different interfacial angles was greater than 40°, failure gradually became apparent due to the influence of the inclination angle. Sliding failure caused by the interface led to the instability and failure of the entire coal–rock combination, which intensified with the increasing angle.

5.2. Fractal Characteristics of Specimen Failure Fragments. In fractal geometry theory, the statistical self-similarity characteristics of the coal and rock specimen crushing process are mainly described by two parameters: fractal dimension and scale-free space. The definition of fractal dimension is as follows:

$$D = -\lim_{\varepsilon \to 0} \frac{\lg N(\varepsilon)}{\lg \varepsilon}, \tag{1}$$

where D is the fractal dimension, ε is a scale, and N is the measurement corresponding to ε.

There are two main methods for calculating the fractal dimension of crushed specimens, which are based on the particle number and particle mass. Both methods use equivalent variable-length pairs to measure particle size and calculate the fractal dimension based on the relationship between feature scale and cumulative quantity.

5.2.1. Particle Number-Based Fractal Dimension. Due to the difficulty in counting the number of fragments smaller than 4.75 mm, the number obtained will not be accurate. Moreover, fragments smaller than 4.75 mm are mainly generated by the friction between crack interfaces or internal compression during compression deformation. In addition, the generation of small fragments is influenced by many factors, including primary fractures and sampling conditions. The above reasons give rise to significant uncertainty in the determination of < 4.75 mm fragments, and the associated research conclusion has little value. Therefore, no research was conducted on the number of fragments < 4.75 mm, and only fragments > 4.75 mm were counted. The length (l), width (w), and thickness (h) of the fragments were measured [44, 45].

The crushed coal body was simplified into a cube, and according to the literature, the equivalent side length L of the cube was calculated using the following formula:

$$L = \sqrt[3]{l \times w \times h}. \tag{2}$$

The formula for calculating fractal dimension is as follows:

$$N = N_0 \left(\frac{L}{L_{\max}} \right) - D, \tag{3}$$

where N is the number of fragments with an equivalent side length $\geq L$, N_0 is the number of fragments with the maximum characteristic size L, and D is the fractal dimension.

For the convenience of drawing and describing the quantitative characteristics of particle size [46–48], logarithmic Equation (3) is reorganized as follows:

$$\lg N = D \lg \left(\frac{L}{L_{\max}} \right) - D \lg N_0. \tag{4}$$

The slope of $\lg N - \lg(\frac{L}{L_{\max}})$ is the fractal dimension. The $\lg N - \lg(\frac{L}{L_{\max}})$ curves of three specimens under different loading rates are shown in Figure 19.

The $\lg N - \lg(\frac{L}{L_{\max}})$ curves of the three differently angled specimens are given in Figure 19. As the loading rate changes

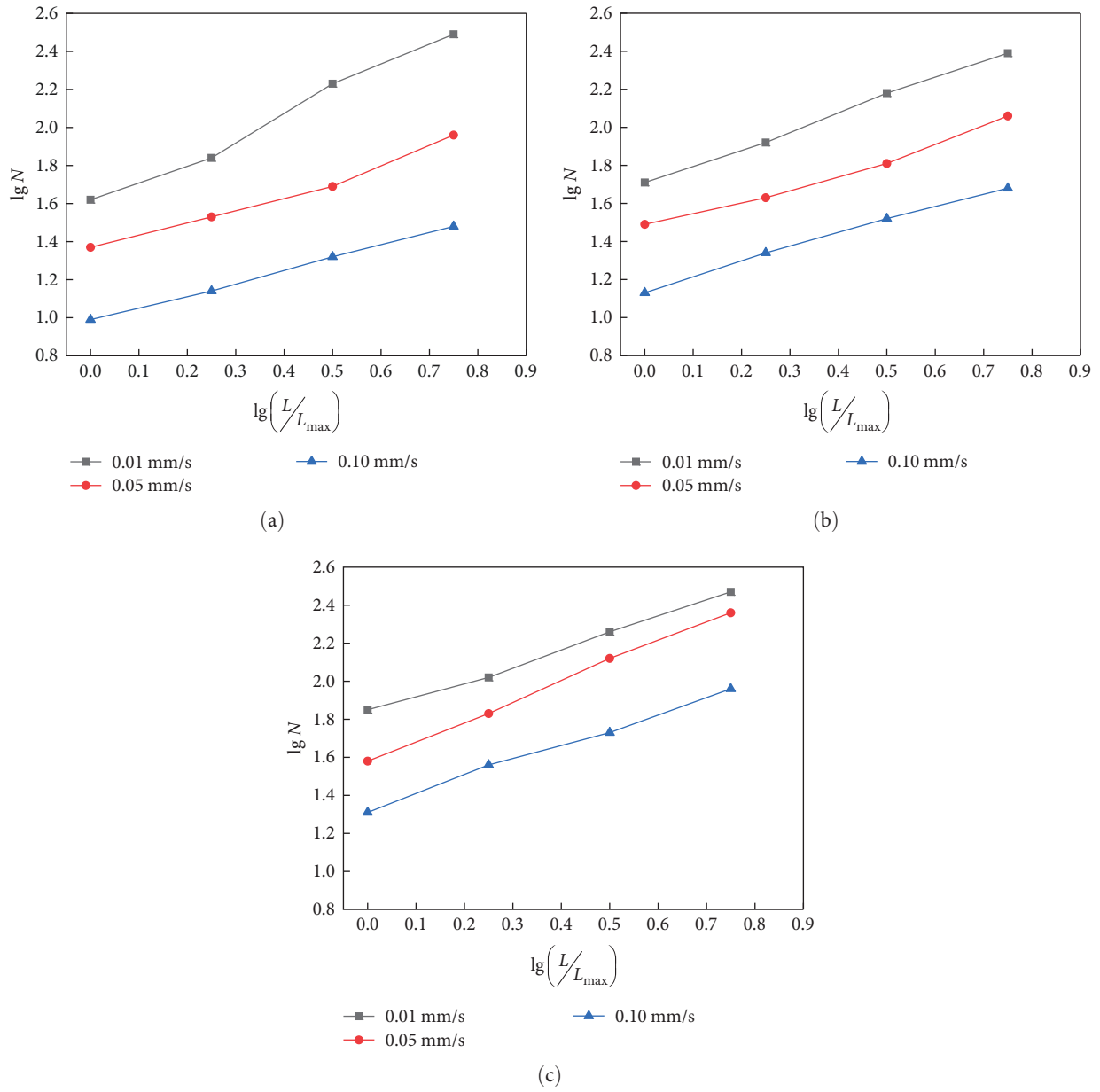

Figure 19: $\lg N - \lg(\frac{L}{L_{max}})$ curves of three specimens under different loading rates: (a) 15°, (b) 30°, and (c) 45°.

from 0.001 to 0.05 to 0.1 mm/s, the coal–rock combination with an inclination angle of 15° has fragments with fractal dimensions of 1.16, 0.79, and 0.65, respectively. The coal–rock combination with an inclination angle of 30° has fractal dimensions of 0.9, 0.76, and 0.73 for the fragments. The coal–rock combination with an inclination angle of 45° has fractal dimensions of 0.82, 1.04, and 0.86 for the fragments. From this, it can be seen that the fractal dimension decreases as the loading rate increases, and the larger the loading rate is, the smaller the fractal dimension. According to the physical significance of the fractal dimension of fragments, the larger the fractal dimension is, the more complex or difficult the fragment is to break, and the more energy it absorbs. When the loading rate is low, the specimen is completely crushed, and more small fragments are formed, which requires more energy consumption. When the loading rate is high, the specimen produces fewer fragments and requires less energy. As the inclination angle increases, the fractal dimension gradually decreases when the loading rate is low. As the loading rate increases, the fractal dimension exhibits a certain degree of dispersion.

5.2.2. Particle Mass-Based Fractal Dimension. The relationship between the particle size and mass distribution of fragments is as follows [49–51]:

$$\frac{M_L}{M} = \left(\frac{L}{a}\right)^k, \tag{5}$$

where M is the total mass of fragments, M_L is the mass of fragments smaller than the equivalent side length L, a is the average size of the fragments, and k is an index.

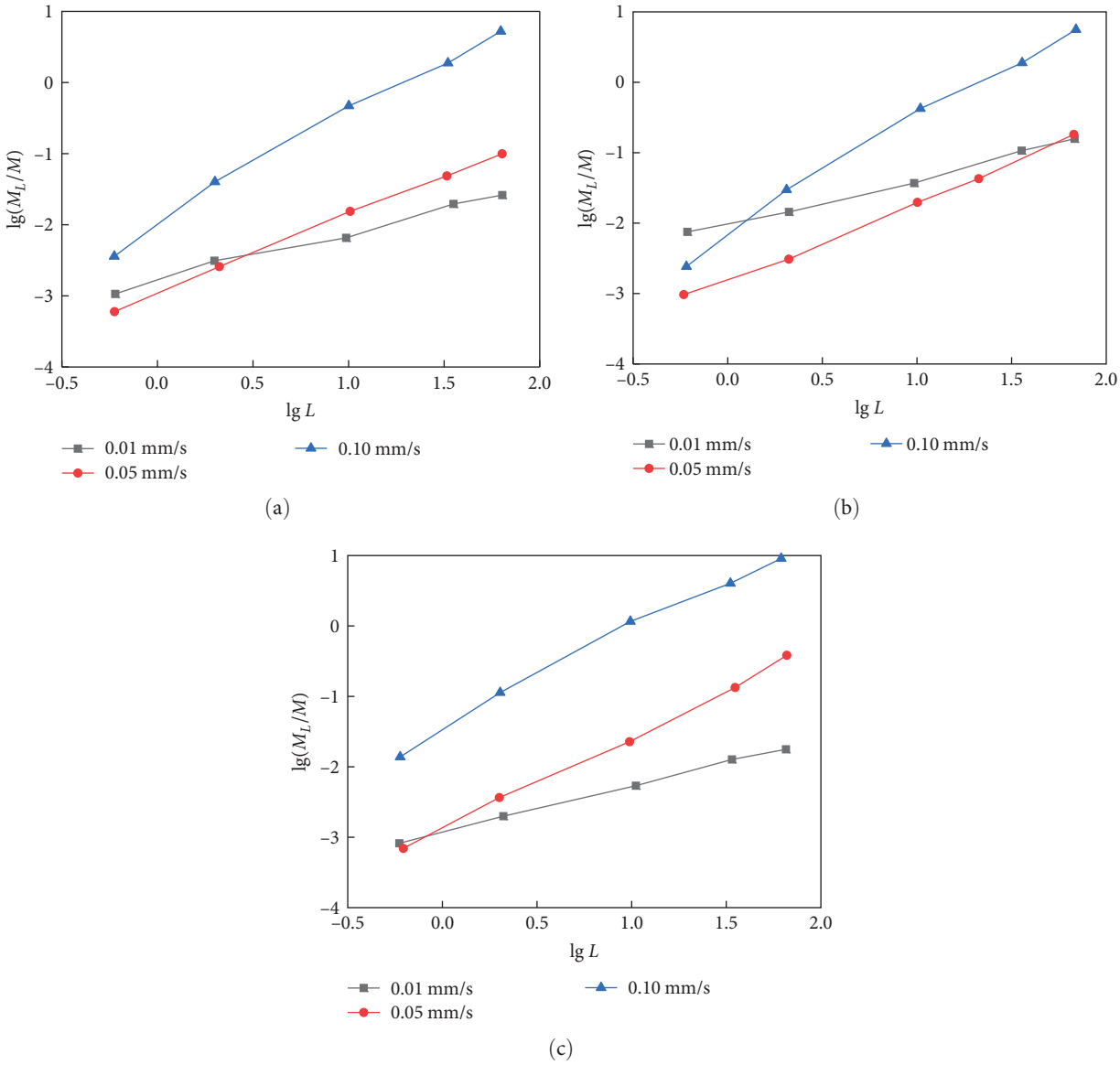

FIGURE 20: $\lg(M_L/M) - \lg L$ curves of three specimens under different loading rates: (a) 15°, (b) 30°, and (c) 45°.

The logarithm of both sides of Formula (5) can be taken to obtain [52–54]:

$$\lg(M_L/M) = k \lg L - k \lg a. \tag{6}$$

According to Equation (6), the slope of the $\lg(M_L/M) - \lg L$ curve is k. According to the fractal theory of rock mechanics, the relationship between the fractal dimension D and the slope k is as follows:

$$D = 3 - k. \tag{7}$$

From Figure 20, it can be seen that the particle mass of the test piece fragments has obvious fractal characteristics. Figure 20 depicts the relationship between the loading rate and fractal dimension. The fractal dimension of the specimens increases with loading rate in the following order: 15° combination: 2.35, 1.93, and 1.48; 30°, combination: 2.36, 1.82, and 1.34; and 45°, combination: 2.34, 1.67, and 1.58. From this perspective, the fractal dimensions of the specimens decrease with increasing loading rate.

5.3. Discussion on the Failure Mechanism of CoalRock Combinations. The failure mechanism of the inclined coal–rock combinations was that the cumulative elastic deformation inside the inclined coal–rock mass reached the energy storage limit. During the compaction stage of the inclined coal–rock mass, the axial deformation of the combination continued to increase, and the internal primary fractures were continuously compressed and closed. In addition, due to the effect of the inclination angle, the friction force at the lowest point of the coal–rock interface continued to increase. In the elastic stage, the axial load of the inclined coal–rock mass further increased, and the friction force

at the lowest point of the composite interface continued to increase; this formed a weak surface, resulting in a significant increase in lateral deformation between the rock mass and the coal mass, weakening the local strength of the coal–rock mass, and initiating internal cracks in the coal–rock mass. Therefore, during the plastic stage, cracks formed and continued to develop and expand at the interface between the coal and rock masses at the lowest point of the interface in the inclined coal–rock combination. When the peak stress was reached, a more obvious crack zone formed here and protruded outwards. In the stages of instability and failure, the area of the fracture zone continued to expand and develop toward the surrounding coal and rock masses, ultimately forming a macroscopic fracture surface that caused the overall instability and failure of the coal and rock masses.

During uniaxial compression of the coal–rock combinations, due to the dip angle of the coal–rock interface, a weak surface formed at the lowest point of the interface due to the downwards force of friction. As a result, the coal–rock mass first fractured at this point and produced cracks, which then expanded and ultimately caused the fracture and instability of the combination.

Due to the large difference between the mechanical properties of sandstone and coal stone, the coal and rock assemblage underwent different deformation when loaded. Under the same load, the axial strain and circumferential strain of the sandstone parts at both ends of the combination body were smaller than those of the coal part. The contact surface between the rock body and the coal body was bonded by high-strength mica adhesive to prevent misalignment of the combination body. The possibility of damage was greatest at the upper and lower edges of coal–rock interface (coal body extrusion friable area), followed by the secondary stress superposition area in the coal and rock bodies. As the vertical force continued to increase, crack penetration caused the stress superposition to gradually increase until the cracks separated the coal body from the rock body, and the damage increased.

The integrity of the specimens after damage differed greatly for different inclination angles. The specimens with angles of 0° and 15° had the best integrity, which explained why the strength of the combinations was close to that of the coal monolith. The main cracks were distributed in the coal body in approximately vertical straight lines, the cracks on the surface of the coal body were densely and uniformly distributed, and there was ring-shaped local expansion. The integrity of the 0° specimen was better; the main cracks were distributed in the coal body, and the angle of the cracks was skewed. For the specimen with a 30° inclination angle, the cracks on the surface of the coal body were more densely distributed, and there were more cracks at the inflection points of the main cracks than in the rock body. The cracks in the specimen with a 45° inclination angle ran through the coal body and the rock body, which mainly corresponded to shear damage. The specimen with a dip angle of 45° had a small slip phenomenon between the coal body and rock body, where it should be noted that the contact surface of the coal and rock bodies was made of a combination of dolomite and adhesive bonding material, and this combination reached the ultimate compressive strength. The coal and rock bodies did not slip directly at the contact surface, but rather within the coal body and the rock body, and there was complete bonding at the contact surface. However, the bottom of the rock body of the 45° specimen was crushed due to the large force. Compared with the 30° specimen, the 45° specimen had an obvious crack running through the coal body and the rock body, and cracking was more extensive in the rock body. For the 30° specimen, the slip phenomenon was minor, but the 45° specimen had a larger slip phenomenon, and slip cracks ran through the coal body and the rock body, mainly corresponding to slip damage accompanied by compression and shear damage. The main cracks were distributed in the coal body, and the inclination angle was large. The cracks on the surface of the coal body were unevenly distributed and mostly concentrated at the inflection points of the main cracks. There was a very obvious outwards bulge in the middle of the coal body, and the cracks produced by the slip damage and shear damage developed and penetrated together to form a macroscopic rupture zone. With increasing inclination angle of the coal–rock assemblage, the uniaxial compressive strength of the assemblage gradually approached the strength of the rock body; the specimen with a large inclination angle had a large degree of rock body damage; and slip damage was produced at inclination angles $\geq 30°$. With increasing specimen load, the coal body entered the plastic stage, and internal cracks started to develop. The stress distribution of the specimens with a small inclination angle of the coal–rock assemblage was uniform, and the degree of crack development was consistent in the cross-section of the coal body. Dense cracks penetrated through the side of the coal body, and local expansion occurred at the interface between the coal and rock. The specimen with a large inclination angle of the coal–rock assemblage underwent stress superposition, which made the penetrating cracks more obvious, especially within the rock body and coal body, and the damage was mainly caused by slipping of the coal and rock contact surface. Specimen damage was mainly due to slip damage at the coal–rock contact surface.

Rock bursts are seismic events that induce sudden and instantaneous destruction of coal and rock bodies and are due to engineering activities such as mining or excavation. The elastic strain energy stored in the rock body is suddenly released, resulting in the blasting of loose material, spalling, ejection, or other damage that constitutes a geological disaster. Rock burst is the most common type of disaster in geotechnical engineering, and it is also an extremely complex problem of rock system movement and stability. Strong impact ground pressure can instantly destroy the whole mine or tunnel, causing many casualties and extensive property loss and even affecting surface buildings. There are many factors affecting the impact ground pressure, such as mining depth, mining in the axial part of an incline or dorsal incline, proximity to the fault structure, the thickness and inclination of the rock layer, an unreasonable mining arrangement, excessive mining speed, and a shift from three-way stress to unidirectional stress. In the simplified impact ground pressure model, the energy is the elastic potential energy stored during the original formation of the coal (rock) body, which is strongly related to the mining

depth; it is also related to geological tectonic stress. However, mining causes the coal (rock) body to lose constraints, and the scale of this loss directly affects the scale of elastic potential energy release of the coal (rock) body. When the inclination angle of the coal body differs at different locations along a section, the greater the inclination angle is, the greater the section thickness, the greater the scale of loss of constraints, and the greater the amount of coal (rock) that participates in the release of elastic potential energy. The inclination angle of the coal seam directly affects the height of the mining face during the mining process, which determines the area of the rock layer that releases elastic potential energy and the scale of energy release. The impact ground pressure model can be simplified by taking the inclination angle of the coal–rock combination as the main influencing factor. When the inclination angle is small, the internal coal (rock) body is prone to tensile damage and slip. When the inclination angle is large, the deformation of the lower rock body is large, and destabilization occurs. The amount of flysch and the amount of energy released increase exponentially and linearly, respectively, with increasing inclination angle, and the elastic potential energy can account for almost all the energy released.

6. Conclusions

(1) Coal and rock samples were taken from the No. 1 Huajin Shaqu Coal Mine in Shanxi Province, and four groups of specimens were prepared according to the different depositional environments. The specimens comprised coal and rock combinations with four inclination angles at 0°, 15°, 30°, and 45°, which were used to simulate coal–rock assemblages in different depositional environments. The experimental results are of great significance to the mining of deep coal–rock mass disturbed by complex high stress and the change of coal seam inclination.

(2) The damage mode of the coal–rock assemblage mainly consisted of inclined shear cracking. The damage was mainly concentrated in the coal body, and there were fine and dense secondary cracks dispersed along the main cracks in the coal body.

(3) As the interfacial angle increased, the cumulative number of acoustic emission events, cumulative energy, peak energy of postpeak damage, and peak amplitude of acoustic emission all decreased. The larger the coal–rock inclination angle was, the larger the number of acoustic emission ringdown signals, and the greater the energy change rate of the composite specimen corresponding to the postpeak stage.

(4) The impact tendency index of the composite specimens was positively correlated with the key acoustic emission parameters, and the number of acoustic emission ringdown signals of the specimens and the rate of change of energy after the stress peak were used as the new criteria.

(5) Fractal theory was used to study the fractal characteristics of the particle number and particle mass of the specimen fragments. The fractal dimension of the particle number decreased with increasing loading rate, and the larger the loading rate was, the smaller the fractal dimension. The fractal dimensions of the particle number and mass of the specimens decreased with increasing loading rate.

Data Availability

The data used to support the findings of this study are available from the corresponding author upon request.

Conflicts of Interest

The authors declare that they have no conflicts of interest regarding the publication of this study.

Authors' Contributions

Yuping Fu contributed in the writing–review and editing; Yongliang He contributed in the supervision, Chuantian Li contributed in the funding acquisition. All authors have read and agreed to the published version of the manuscript.

Acknowledgments

This research was supported by the Fundamental Research Program of Shanxi Province (202203021222184), the Natural Science Foundation of Shanxi, the Taiyuan University of Science and Technology Scientific Research Initial Funding (20222112), and the Reward Fund for Excellent Doctors Working in Shanxi Province (20232039).

References

[1] T. Shuheng, S. Shenglin, Q. Yong, J. Yaofa, and W. Wenfeng, "Distribution characteristics of sulfur and the main harmful trace elements in China's coal," *Acta Geologica Sinica - English Edition*, vol. 82, no. 3, pp. 722–730, 2008.

[2] X. Li, Y. Lu, Y. Shi et al., "Effects of urbanization on the distribution of polycyclic aromatic hydrocarbons in China's estuarine rivers," *Environmental Pollution*, vol. 301, Article ID 119001, 2022.

[3] Z. Tao, S. Luo, Y. Qiao, and M. He, "Key factors analysis and constitutive equation modification of a macro-NPR bolt for achieving high constant resistance and large deformation characteristics," *International Journal of Rock Mechanics and Mining Sciences*, vol. 147, Article ID 104911, 2021.

[4] W. Sun and S. Zhang, "Development of floor water invasion of mining influence simulation testing system and its application," *Chinese Journal of Rock Mechanics and Engineering*, vol. 34, no. 1, pp. 3274–3280, 2015.

[5] Y. Zheng, C. Zhai, J. Zhang et al., "Deformation and fracture behavior of strong–weak coupling structure and its application in coal roadway instability prevention," *Fatigue & Fracture of Engineering Materials & Structures*, vol. 45, no. 1, pp. 203–221, 2022.

[6] J. Wang, Q. Zhang, J. Zhang, H. Liu, G. Zhu, and Y. Wang, "Study on the controller factors associated with roof falling and ribs spalling in deep mine with great mining height and compound roof," *Engineering Failure Analysis*, vol. 129, Article ID 105723, 2021.

[7] L. Xu, K. Lu, Y. Pan, and Z. Qin, "Study on rock burst characteristics of coal mine roadway in China," *Energy Sources, Part A: Recovery, Utilization, and Environmental Effects*, vol. 44, no. 2, pp. 3016–3035, 2022.

[8] J. Lu, D. Zhang, G. Huang, X. Li, H. Gao, and G. Yin, "Effects of loading rate on the compound dynamic disaster in deep underground coal mine under true triaxial stress," *International Journal of Rock Mechanics and Mining Sciences*, vol. 134, Article ID 104453, 2020.

[9] Z. Cui, Q. Sheng, X. Leng, Z. Zhu, and Y. Zhang, "Estimation of the mechanical properties of igneous rocks in consideration of seismic effects," *Rock Mechanics and Rock Engineering*, vol. 52, no. 11, pp. 4287–4300, 2019.

[10] P.-Q. Qiu, J.-G. Ning, J. Wang, S.-C. Hu, and Z. Li, "Mitigating rock burst hazard in deep coal mines insight from dredging concentrated stress: a case study," *Tunnelling and Underground Space Technology*, vol. 115, Article ID 104060, 2021.

[11] L. Hu, Y. Zhang, Z. Huang, Q. Li, H. Wang, and Z. Hu, "Coal–rock dynamic disaster prevention mechanism based on the dual loads of dynamic barrier and static pressure relief by hydraulic slotting," *ACS Omega*, vol. 8, no. 8, pp. 7639–7647, 2023.

[12] M. E. Ahmadi, S. Mesroghli, B. Hedayat, H. Nazerian, A. Shirazi, and A. Shirazy, "Assessment of the influence of sulfuric acid/hydrogen peroxide mixture on organic sulfur reduction of high sulfur coals and their chemical composition," *Open Journal of Geology*, vol. 12, no. 3, pp. 199–214, 2022.

[13] Z. Wei, K. Yang, X.-L. Chi, X. He, X.-Y. Zhao, and J.-Q. Zhang, "Dynamic tensile properties, deformation, and failure testing of impact-loaded coal samples with various water content," *Scientific Reports*, vol. 11, Article ID 7096, 2021.

[14] W. Li, J. Bai, J. Cheng, S. Peng, and H. Liu, "Determination of coal–rock interface strength by laboratory direct shear tests under constant normal load," *International Journal of Rock Mechanics and Mining Sciences*, vol. 77, pp. 60–67, 2015.

[15] X. S. Liu, Y. L. Tan, J. G. Ning, Y. W. Lu, and Q. H. Gu, "Mechanical properties and damage constitutive model of coal in coal–rock combined body," *International Journal of Rock Mechanics and Mining Sciences*, vol. 110, pp. 140–150, 2018.

[16] P. Jin, E. Wang, and D. Song, "Study on correlation of acoustic emission and plastic strain based on coal–rock damage theory," *Geomechanics and Engineering*, vol. 12, no. 4, pp. 627–637, 2017.

[17] Q. Ma, Y.-L. Tan, X.-S. Liu, Z.-H. Zhao, and D.-Y. Fan, "Mechanical and energy characteristics of coal–rock composite sample with different height ratios: a numerical study based on particle flow code," *Environmental Earth Sciences*, vol. 80, Article ID 309, 2021.

[18] X. Wang, K.-X. Hu, L. Zhang, X. Yu, and E.-J. Ding, "Characterization and classification of coals and rocks using terahertz time-domain spectroscopy," *Journal of Infrared, Millimeter, and Terahertz Waves*, vol. 38, pp. 248–260, 2017.

[19] D. Guo, W. Zhang, Q. Chen, and Z. Wang, "Failure mechanism and acoustic emission characteristics of coal–rock samples," *Journal of Mining Science*, vol. 58, no. 3, pp. 390–397, 2022.

[20] T. Wang, Z. Ma, P. Gong, N. Li, and S. Cheng, "Analysis of failure characteristics and strength criterion of coal–rock combined body with different height ratios," *Advances in Civil Engineering*, vol. 2020, Article ID 8842206, 14 pages, 2020.

[21] B. Huang and J. Liu, "The effect of loading rate on the behavior of samples composed of coal and rock," *International Journal of Rock Mechanics and Mining Sciences*, vol. 61, pp. 23–30, 2013.

[22] C. Ma, C. Zhu, J. Zhou, J. Ren, and Q. Yu, "Dynamic response and failure characteristics of combined rocks under confining pressure," *Scientific Reports*, vol. 12, no. 1, pp. 1–12, 2022.

[23] H. Zhang and F. Wang, "Experimental study on creep characteristics of infiltrated coal–rock under load," *Archive of Applied Mechanics*, vol. 40, pp. 1–14, 2022.

[24] H. Li, S. Sun, L. Wang, J. Liu, and Z. Zhang, "Damage law and mechanism of coal–rock joint structure induced by liquid nitrogen at low temperature," *Scientific Reports*, vol. 12, Article ID 10901, 2022.

[25] H. Zhang, C.-P. Lu, B. Liu, Y. Liu, N. Zhang, and H.-Y. Wang, "Numerical investigation on crack development and energy evolution of stressed coal–rock combination," *International Journal of Rock Mechanics and Mining Sciences*, vol. 133, Article ID 104417, 2020.

[26] F. Q. Gong, H. Ye, and Y. Luo, "The effect of high loading rate on the behaviour and mechanical properties of coal–rock combined body," *Shock and Vibration*, vol. 2018, Article ID 4374530, 9 pages, 2018.

[27] F. Lu, G. Zhang, Y. Ding, and Y. Gan, "Dynamic-difference based generative adversarial network for coal–rock fracture evolution prediction," *IET Image Processing*, vol. 16, no. 14, pp. 3737–3747, 2022.

[28] Z. Wu, L. Li, Y. Lou, and W. Wang, "Energy evolution analysis of coal fracture damage process based on digital image processing," *Applied Sciences*, vol. 12, no. 8, Article ID 3944, 2022.

[29] Z.-G. Xia, S. Liu, Z. Bian, J. Song, F. Feng, and N. Jiang, "Mechanical properties and damage characteristics of coal–rock combination with different dip angles," *KSCE Journal of Civil Engineering*, vol. 25, pp. 1687–1699, 2021.

[30] W. Tian, K. Yang, S. Wu et al., "Impact of hydration on the mechanical properties and damage mechanisms of natural silk fibre reinforced composites," *Composites Part A: Applied Science and Manufacturing*, vol. 147, Article ID 106458, 2021.

[31] M. A. Mattoni, J. Y. Yang, C. G. Levi, and F. W. Zok, "Effects of matrix porosity on the mechanical properties of a porous-matrix, all-oxide ceramic composite," *Journal of the American Ceramic Society*, vol. 84, no. 11, pp. 2594–2602, 2001.

[32] P. Xiao, D. Li, G. Zhao, and H. Liu, "New criterion for the spalling failure of deep rock engineering based on energy release," *International Journal of Rock Mechanics and Mining Sciences*, vol. 148, Article ID 104943, 2021.

[33] X. F. Xu, L. M. Dou, C. P. Lu, and Y. L. Zhang, "Frequency spectrum analysis on micro-seismic signal of rock bursts induced by dynamic disturbance," *Mining Science and Technology (China)*, vol. 20, no. 5, pp. 682–685, 2010.

[34] D. Huang, X. Chang, Y. Tan, K. Fang, and Y. Yin, "From rock microstructure to macromechanical properties based on fractal dimensions," *Advances in Mechanical Engineering*, vol. 11, no. 3, pp. 1–13, 2019.

[35] X. B. Li, M. Luo, and J. P. Liu, "Fractal characteristics based on different statistical objects of process-based digital rock models," *Journal of Petroleum Science and Engineering*, vol. 179, pp. 19–30, 2019.

[36] W. He, A. Hayatdavoudi, H. Shi, K. Sawant, and P. Huang, "A preliminary fractal interpretation of effects of grain size and grain shape on rock strength," *Rock Mechanics and Rock Engineering*, vol. 52, pp. 1745–1765, 2019.

[37] S. Dewangan and S. Chattopadhyaya, "Critical analysis of wear mechanisms in cemented carbide," *Journal of Materials*

Engineering and Performance, vol. 24, no. 7, pp. 2628–2636, 2015.

[38] T. Otomo, N. Taguchi, and E. Kasai, "Suppression of the formation of large pores in the assimilated parts of sinter produced using pisolitic ores," *ISIJ International*, vol. 36, no. 11, pp. 1338–1343, 1996.

[39] W. Guo, D. Zhang, T. Zhao et al., "Influence of rock strength on the mechanical characteristics and energy evolution law of gypsum–rock combination specimen under cyclic loading–unloading condition," *International Journal of Geomechanics*, vol. 22, no. 5, pp. 1–22, 2022.

[40] Z. Zhao, K. Zhao, and X. Wang, "Study on mechanical characteristics and damage evolution law of coal–rock-like under different loading rates," *Coal Science and Technology*, vol. 45, no. 10, pp. 41–47, 2017.

[41] Q. Meng, M. Zhang, L. Han, H. Pu, and Y. Chen, "Acoustic emission characteristics of red sandstone specimens under uniaxial cyclic loading and unloading compression," *Rock Mechanics and Rock Engineering*, vol. 51, pp. 969–988, 2018.

[42] Y. Zhou, C. Liu, and D. Ma, "Method improvement and effect analysis of triaxial compression acoustic emission test for coal and rock," *Advances in Civil Engineering*, vol. 2019, Article ID 8910362, 10 pages, 2019.

[43] Z. Su, K. Geng, F. Zhou, J. Sun, and H. Yu, "Influence of freeze-thaw cycles on acoustic emission characteristics of granite samples under triaxial compression," *Advances in Civil Engineering*, vol. 2021, Article ID 5571680, 11 pages, 2021.

[44] Y. Y. Li, S. C. Zhang, Z. J. Wen et al., "Energy conversion and fragment distribution characteristics of coal sample under uniaxi-alcyclic loading," *Journal of China Coal Society*, vol. 44, no. 5, pp. 1411–1420, 2019.

[45] D. D. Li, X. N. Jia, J. L. Miao, and M. C. He, "Analysis of ractal characteristics of fragment from rockburst test of granite," *Chinese Journal of Rock Mechanics and Engineering*, vol. 29, no. S1, pp. 3280–3289, 2010.

[46] C. A. Alves, A. M. P. Vicente, A. I. Calvo et al., "Physical and chemical properties of non-exhaust particles generated from wear between pavements and tyres," *Atmospheric Environment*, vol. 224, Article ID 117252, 2020.

[47] K. S. Shah, M. H. b. M. Hashim, M. Z. Emad, K. S. b. Ariffin, M. Junaid, and N. M. Khan, "Effect of particle morphology on mechanical behavior of rock mass," *Arabian Journal of Geosciences*, vol. 13, Article ID 708, 2020.

[48] A. Rispoli, A. M. Ferrero, M. Cardu, and A. Farinetti, "Determining the particle size of debris from a tunnel boring machine through photographic analysis and comparison between excavation performance and rock mass properties," *Rock Mechanics and Rock Engineering*, vol. 50, pp. 2805–2816, 2017.

[49] B. Hazra, D. Chandra, A. K. Singh et al., "Comparative pore structural attributes and fractal dimensions of lower Permian organic-matter-bearing sediments of two Indian basins: inferences from nitrogen gas adsorption," *Energy Sources, Part A: Recovery, Utilization, and Environmental Effects*, vol. 41, no. 24, pp. 2975–2988, 2019.

[50] B. Hazra, D. A. Wood, P. K. Singh et al., "Source rock properties and pore structural framework of the gas-prone lower Permian shales in the Jharia basin, India," *Arabian Journal of Geosciences*, vol. 13, Article ID 507, 2020.

[51] M. J. Munawar, S. Vega, C. Lin, M. Alsuwaidi, N. Ahsan, and R. R. Bhakta, "Upscaling reservoir rock porosity by fractal dimension using three-dimensional micro-computed tomography and two-dimensional scanning electron microscope images," *Journal of Energy Resources Technology*, vol. 143, no. 1, Article ID 013003, 2021.

[52] Z. Zhang, G. Liu, P. Chang, X. Wang, and J. Lin, "Fractal characteristics for coal chemical structure: principle, methodology and implication," *Chaos, Solitons & Fractals*, vol. 173, Article ID 113699, 2023.

[53] Z. Zhang, G. F. Liu, X. M. Wang, H. Liu, and B. L. Li, "Fractal characterization on fracture volume in coal based on CT scanning: principle, methodology and implication," *Fractals*, vol. 30, no. 6, Article ID 2250124, 2022.

[54] Z. Zhang, G. F. Liu, X. M. Wang, M. S. Wang, B. L. Li, and H. Liu, "Fractal characterization on three-dimensional fracture tortuosity in coal based on CT Scanning," *Fractals*, vol. 31, no. 5, Article ID 2350034, 2023.